

Unsupervised single-particle deep classification via statistical manifold learning

Jiayi Wu^{1,2}, Yongbei Ma², Charles Condgon³, Bevin Brett³, Shuobing Chen^{1,2}, Qi Ouyang^{1,5}, Youdong Mao^{1,2,4,5*}

¹State Key Laboratory for Mesoscopic Physics, Institute of Condense Matter Physics, School of Physics, Peking University, Beijing 100871, China.

²Intel Parallel Computing Center for Structural Biology, Dana-Farber Cancer Institute, Boston, MA 02215, USA.

³Software and Services Group, Intel Corporation, Santa Clara, CA 95052, USA.

⁴Department of Microbiology and Immunobiology, Harvard Medical School, Boston, MA 02115, USA.

⁵Center for Quantitative Biology, Peking-Tsinghua Center for Life Sciences, Peking University, Beijing, China

*Correspondence should be addressed to Y.M. Tel: +1 617 632 4358. Fax: +1 617 632 4338.

E-mail address: youdong_mao@dfci.harvard.edu

Structural heterogeneity in single-particle images presents a major challenge for high-resolution cryo-electron microscopy (cryo-EM) structure determination. Here we introduce a statistical manifold learning approach for unsupervised single-particle deep classification. When optimized for Intel high-performance computing (HPC) processors, our approach can generate thousands of reference-free class averages within several hours from hundreds of thousands of single-particle cryo-EM images. Deep classification thus assists in computational purification of single-particle datasets for high-resolution reconstruction.

Single-particle cryo-EM is emerging as a mainstream tool to visualize the three-dimensional (3D) structures of biomolecules in their native functional states at near-atomic resolution^{1,2}. Individual biomolecules may sample multiple conformations. Thus a prerequisite for high-resolution structure determination is to obtain a ‘pure’ dataset that includes particle images in an identical conformational state³. To distinguish different conformations in raw particle images, reference-free two-dimensional (2D) classification is commonly practiced as the first step in evaluation of structural heterogeneity², or used as an intermediate step during the iterations between 2D and 3D classifications for *in silico* purification⁴.

There are two major existing approaches of reference-free 2D classification of single-particles: (1) K-means clustering following reference-free alignment through cross-correlation (CC) and multivariate statistical analysis (MSA)², and (2) unsupervised maximum-likelihood (ML) or *maximum a posteriori* (MAP) classification⁵⁻⁷. In the former approach, the classification accuracy is affected by the noise-induced misalignment resulting from false peaks in cross-correlation calculation. Its performance dramatically reduces as the signal-to-noise ratio (SNR) decreases. By contrast, the ML-based approach explores optimal probability in measuring image

similarity, and exhibits robust resistance to the noise-induced misalignment⁵. However, a prominent drawback lies in that the likelihood matching insufficiently differentiates structural heterogeneity among similar but critically different views. In each ML-classified group of single-particles one could find a mixture of heterogeneous 2D projection structures with a large variation in likelihood. This effect causes a decrease in the effective number of classes while increasing the cycles of ML optimization. To date, there has been a lack of reference-free classification methods that can efficiently sort out highly heterogeneous single-particles into thousands of homogenous 2D classes while still keeping computation efficient.

Here we introduce a reference-free deep classification method based on statistical manifold learning (SML)⁸⁻¹⁰. We implemented SML-based classification in a software package named ROME (Refinement and Optimization based on Machine Learning), which was optimized for both Intel[®] Xeon[®] multi-core processors and Intel[®] Many-Integrated Core (MIC) Architecture¹¹ to enable efficient computation of thousands of reference-free class averages in a highly affordable fashion. We tested our approach with several cryo-EM datasets to demonstrate the advantage of deep classification in discerning subtle structural differences directly in 2D class averages corresponding to distinct conformations.

Our SML algorithm is derived from a generative topographic mapping (GTM) algorithm framework that defines a nonlinear, parametric mapping $\mathbf{y}(\mathbf{x}; \mathbf{W})$ from a low-dimensional latent variable space to a high-dimensional data space⁸ (**Fig. 1a**). $\mathbf{y}(\mathbf{x}; \mathbf{W})$ is reconstituted by a set of basis functions through a weight matrix \mathbf{W} . The latent variables associated with 2D structural difference, arising from either different orientations or distinct conformational states of the imaged biomolecules, is enumerated evenly in the latent space. To efficiently correct the effect of the contrast transfer function² (CTF), we consider the nonlinear mapping problem directly in

Fourier or reciprocal space. Thus, a vector in data space represents the Fourier transform of a particle image. A low-dimensional non-Euclidean manifold, composed of the observed vectors in data space, is nonlinearly mapped from the latent space and embedded into the higher dimensional data space. The *maximum a posteriori* (MAP) estimator for the nonlinear mapping is expressed as $Q(\Theta) = \sum_{n=1}^N \sum_{k=1}^K r_{kn}(\Theta) \ln[p(\mathbf{t}_n | \mathbf{x}_k, \mathbf{W}, \beta) p(\mathbf{x}_k)]$, where $r_{kn}(\Theta)$ represents the posterior probability or responsibility that the data point $\mathbf{t}_n = \mathbf{y}_n(\mathbf{x}_k; \mathbf{W})$ was generated by the latent variable \mathbf{x}_k under a given set of model parameters Θ , including the weight matrix \mathbf{W} , the variance of noise β , the variance of Gaussian basis functions and the variance of Gaussian prior over the weights \mathbf{W} . $p(\mathbf{t}_n | \mathbf{x}_k, \mathbf{W}, \beta)$ represents the probability that the latent variable \mathbf{t}_n is mapped to the data point \mathbf{x}_k on the embedded manifold; and $p(\mathbf{x}_k)$ represents the prior probability distribution of \mathbf{x}_k on the latent variable space. Thus, the problem of unsupervised classification can be translated into the maximization of the MAP estimator of the nonlinear, probabilistic manifold embedding.

The unsupervised classification problem is ill posed because of a high level of noise, potentially missing orientations and discontinuity between different conformational states in the single-particle cryo-EM data. To enable effective computation, the expectation-maximization algorithm is employed to find the model parameters Θ corresponding to an optimal classification. The inclusion of the CTF effect invalidates the original matrix operation formulae in the expectation-maximization solution of GTM⁸. Thus, a new set of mathematical equations were developed for the expectation-maximization algorithm that can properly classify images based on the true 2D structural difference instead of the difference in the CTF effect caused by

defocus variation (see Methods for mathematical details). Upon convergence of the expectation-maximization algorithm, one can obtain the posterior probability r_{kn} of the n -th image for given

k -th class. The class average is thus given by $A_{kd} = \frac{\sum_{n=1}^N r_{kn}(\Theta)\beta_{nd}CTF_{nd}t_{nd}}{\sum_{n=1}^N r_{kn}(\Theta)\beta_{nd}CTF_{nd}t_{nd}^2 + \alpha}$, where A_{kd}

represents the d -th pixel intensity of the k -th class average, CTF_{nd} represents the d -th component of contrast transfer function for the n -th image, β_{nd} represents the d -th component of noise standard deviation for the n th image, and α represents the variance of the prior. Previous work has established GTM as an alternative to self-organizing maps¹² (SOM) and that the GTM framework overcomes most limitations in the SOM while introducing no significant disadvantages^{8,9}.

Although SML-based algorithm may excel in unsupervised deep classification, it is not computationally efficient in image alignment, a procedure that determines three geometrical parameters for each image: x - y translational shifts and in-plan rotation. Thus, we employed the adaptive MAP method^{7,13} to align single-particle images prior to SML-based classification (**Fig. 1b**). Averages from random subsets of unaligned images are used to initialize the MAP-based image alignment. Further, a Gaussian model was used to initialize all the parameters of expectation-maximization algorithm in SML solution. Thus, in both the steps of MAP-based alignment and SML-based classification, no external initial model or reference is used, ensuring the unsupervised nature of our approach.

To demonstrate the applicability of our deep classification approach, we applied our method to several experimental cryo-EM data (**Supplementary Fig. 1**). First, ROME was used for an

unsupervised classification on a 17,103-particle dataset of the inflammasome complex⁴. The resulting class averages directly reveal three different conformations of the complexes corresponding to 10-, 11- and 12-fold symmetry (**Fig. 2a**). For comparison, 300 classes were produced by 2D reference-free MAP classification implemented in RELION¹⁴ (**Supplementary Fig. 2**). Second, unsupervised deep SML classification of 96,488 particles of proteasomal RP-CP (regulatory particle associated with core particle) sub-complex directly reveals different local features among class averages (**Fig. 2b**). These local differences were verified to correspond to distinct conformational states through further 3D reconstruction. Our results indicate that deep classification can sort out not only the projections of underlying structure into relatively homogenous 2D classes but also unearth incomplete structure or junk particles, allowing efficient *in silico* purification of single-particle datasets.

Unsupervised classification with improved accuracy can help identify hidden heterogeneity in the reference-free classes generated by other methods. For instance, after initial reference-free classification, particle images of specific classes could be selected for a deeper unsupervised classification by SML. Delicate difference between SML-generated class averages might also reveal features corresponding to distinct conformational states. 843 particles in one class resulting from MAP-based classification (**Fig. 2c**), whose average visually looks like the side view of 11-fold inflammasome complex, are classified into 50 sub-classes by SML (**Supplementary Fig. 3**). Based on the length of the intrinsic structure, the SML-based reference-free classification identified the side-view projection of 10-fold inflammasome complex among the 50 sub-classes (the red boxes in **Fig. 2d**), suggesting the MAP-generated initial class is mixed by the complexes with both 10-fold and 11-fold symmetry. Another classified image group with 3961 particles, whose average visually looks like a tilt view of the

free 19S regulatory particle (RP) that is not associated with a 20S core particle (CP), was further classified by SML (**Fig. 2e**). The deeper classification identified 448 single-particle images of RP-CP sub-complexes that are mis-classified into the dataset of free RP (**Fig. 2f**). Comparison with other algorithms including MAP and K-means clustering suggests that our SML outperforms these algorithms in unambiguously identifying hidden heterogeneity in the initially classified data groups (**Supplementary Fig. 3**).

Our implementation of SML-based deep classification algorithm in ROME software system has been optimized for modern CPU technology such as Intel[®] MIC Architecture that is used in the Intel Xeon Phi Knights Corner and Knight Landing processors. Our modernized code in ROME outperforms the existing software in both speed and magnitude. First, we compared the computational performance between ROME and RELION with several datasets of different particle numbers. It took 143 minutes for ROME to classify 57,001 particles of RP into 300 unsupervised classes on a computing cluster of 512 Intel Xeon E5 CPU cores (**Fig. 3a**). By contrast, it took 2379 minutes for RELION to classify the same dataset into 300 unsupervised classes on the same cluster. In all cases, the expectation-maximization was run for 30 rounds. Thus, under the same circumstance, ROME exhibits about 10-20 times speedup compared to RELION in unsupervised 2D classification. Second, a 96,488-particle dataset of RP complex was used to benchmark the performance of unsupervised classification in ROME with different class numbers on the 512-core computing cluster (**Fig. 3b**). With increasing the class number from 100 to 1000, the running time of SML classification is increased in a polynomial behavior from 14 to 214 minutes. Specifically, ROME completed unsupervised classification of 1000 classes in 306 minutes with 30-round of expectation-maximization (**Supplementary Fig. 4**), whereas RELION won't complete the same rounds of optimization in a week on the same

hardware condition. For more comparison, we also used this dataset to test reference-free classification on 1000-class level by MSA and K-means clustering in SPIDER¹⁵. Unfortunately, the program kernel was dumped upon a crash in the reference-free alignment step. More benchmark details of ROME are provided in **Supplementary Table 1**.

Unsupervised 2D classification plays an important role in high-resolution structure determination by single-particle cryo-EM. SML-based deep classification following MAP-based image alignment, implemented in an open-source software ROME, exhibits an unprecedented capability in obtaining thousands of reference-free class averages in several hours. Applications to experimental datasets demonstrate that unsupervised deep classification by ROME is highly effective in distinguishing structural heterogeneity among single-particle datasets. This can in turn, when used iteratively with 3D classification, help in improving structural homogeneity of cryo-EM datasets, which has been already used for high-resolution refinement in our recent work⁴.

Acknowledgements

The authors thank J. Jackson and T. Song for assistance in maintaining the high-performance computing system. The experiments were performed in part at the Center for Nanoscale Systems at Harvard University, a member of the National Nanotechnology Infrastructure Network (NNIN), which is supported by the National Science Foundation under NSF award no. ECS-0335765. This work was funded by research funds at Peking University, by the Intel Parallel Computing Center program, and by gifts from Mr. and Mrs. Daniel J. Sullivan, Jr..

Online Methods

Mathematical model for statistical manifold learning. The goal of generative topographic mapping (GTM) is to find a representation for the distribution $p(\mathbf{t})$ of data in a D -dimensional space $\mathbf{t} = (t_1, \dots, t_D)$ in terms of a number of L -dimensional latent variables $\mathbf{x} = (x_1, \dots, x_L)$. This is achieved through a nonlinear, parametric mapping $\mathbf{y}(\mathbf{x}; \mathbf{W})$ from a L -dimensional latent variable space to a D -dimensional data space. For single-particle analysis of cryo-EM data, where the molecule is free to assume any orientations while sampling an unknown number of conformational states, a range of latent variables representing candidate class identities are among a set of discrete points enumerated evenly in the latent space. A vector in the data space represents the product of the Fourier transform of each single-particle image multiplied by the corresponding CTF of the image. GTM used in this work relies on embedding a low-dimensional manifold mapped from the latent space into the higher dimensional data space.

In the latent space, all possible variables were enumerated. Here we suppose the probability distribution in the latent space $p(\mathbf{x})$ to be a particular uniform form. If we set K points in the latent space, then the probability distribution $p(\mathbf{x})$ is made up by summation of K equally weighted delta functions

$$p(\mathbf{x}) = \frac{1}{K} \sum_{k=1}^K \delta(\mathbf{x} - \mathbf{x}_k). \quad (1)$$

In data space, each experimental data point is represented a D -dimensional vector \mathbf{t}_n , whose components are d -th pixel intensity value of cryo-EM data. We mapped every regular grids in the latent space to the data space as $\mathbf{y}(\mathbf{x}; \mathbf{W})$ to represent the unknown projection of each underlying class. Based on a white noise assumption, we convolute the probability distribution in data space

with isotropic Gaussian noise distribution, given by

$$p(\mathbf{t}_n | \mathbf{x}_k, \mathbf{W}, \beta) = \prod_d^D \left(\frac{\beta_{nd}}{2\pi} \right)^{\frac{1}{2}} \exp \left\{ -\frac{\beta_{nd}}{2} \left(t_{nd} - CTF_{nd} \sum_m^M \varphi_m(\mathbf{x}_k) W_{md} \right)^2 \right\}, \quad (2)$$

where \mathbf{t}_n denotes the n -th single-particle image, t_{nd} denotes intensity of the d -th pixel of the n -th image, β denotes the variance of noise and y_d denotes the intensity of d -th pixel of underlying class. This mapping embeds a manifold from the latent space into the data space. The manifold can reflect the geometry of the latent space, which means that the underlying classification information can be reflected by this embedded manifold. For mapping form $\mathbf{y}(\mathbf{x}; \mathbf{W})$ in GTM, a normally generalized linear regression model was chosen. So the form of $\mathbf{y}(\mathbf{x}; \mathbf{W})$ can be specified by a set of basis functions $\{\varphi_m\}$

$$y_d(\mathbf{x}_k, \mathbf{W}) = \sum_m^M \varphi_m(\mathbf{x}_k) W_{md}, \quad (3)$$

Here \mathbf{W} is the weight matrix. We use a combination of one fixed basis function and several Gaussians basis functions in the form

$$\varphi_m(\mathbf{x}_k) = \begin{cases} \exp \left\{ -\frac{\|\mathbf{x}_k - \boldsymbol{\mu}_m\|^2}{2\sigma^2} \right\}, & m \leq M_{NL} \\ 1, & m = M_{NL} + 1 \end{cases}. \quad (4)$$

Here M_{NL} denotes the number of Gaussian basis functions, $\boldsymbol{\mu}_m$ denotes the mean of the Gaussian distribution and σ denotes the common variance of the Gaussian distribution. By integrating over the manifold, the probability of experimental data for given all parameters in data space is

$$p(\mathbf{t} | \mathbf{W}, \beta) = \int p(\mathbf{t} | \mathbf{x}, \mathbf{W}, \beta) p(\mathbf{x}) d\mathbf{x}. \quad (5)$$

From equation (1), the integral will be turned into a sum,

$$p(\mathbf{t}|\mathbf{W}, \beta) = \int p(\mathbf{t}|\mathbf{x}, \mathbf{W}, \beta) p(\mathbf{x}) d\mathbf{x} = \frac{1}{K} \sum_{k=1}^K p(\mathbf{t}|\mathbf{x}_k, \mathbf{W}, \beta). \quad (6)$$

Thus given a finite set of N cryo-EM images $(\mathbf{t}_1, \mathbf{t}_2, \dots, \mathbf{t}_N)$, we can calculate the likelihood function of this model,

$$L = \prod_{n=1}^N p(\mathbf{t}_n|\mathbf{W}, \beta) = \prod_{n=1}^N \left[\frac{1}{K} \sum_{k=1}^K p(\mathbf{t}_n|\mathbf{W}, \beta) \right]. \quad (7)$$

For convenience, we use log-likelihood function and maximize it with respect to \mathbf{W} and β

$$L = \sum_n \ln \left(\frac{1}{K} \sum_k p(\mathbf{t}_n|\mathbf{x}_k, \mathbf{W}, \beta) \right). \quad (8)$$

Expectation-maximization algorithm in statistical manifold learning. Unfortunately, only experimental data \mathbf{t} are known. To find the hidden variables, one needs to use the expectation-maximization algorithm to maximize the log-likelihood function regularized with a prior over \mathbf{W} . A regularized maximum-likelihood estimator is more formally called the MAP (*maximum a posteriori*) estimator. In the expectation step (E-step), one calculates the responsibility of latent space point for given data points and all parameters \mathbf{W} and β .

$$r_{kn} = p(\mathbf{x}_k|\mathbf{t}_n, \mathbf{W}, \beta) = \frac{p(\mathbf{t}_n|\mathbf{x}_k, \mathbf{W}, \beta) p(\mathbf{x}_k)}{\sum_{k'} p(\mathbf{t}_n|\mathbf{x}_{k'}, \mathbf{W}, \beta) p(\mathbf{x}_{k'})}. \quad (9)$$

Here r_{kn} represents the posterior probability that the n -th data point was generated by k -th latent point. The weighted MAP function was built

$$Q(\Theta, \Theta^i) = \sum_{n=1}^N \sum_{k=1}^K r_{kn}(\Theta^i) \ln[p(\mathbf{t}_n|\mathbf{x}_k, \mathbf{W}, \beta) p(\mathbf{x}_k)] = \sum_{n=1}^N \sum_{k=1}^K r_{kn}(\Theta^i) \ln \left[\frac{1}{K} \sum_k p(\mathbf{t}_n|\mathbf{x}_k, \mathbf{W}, \beta) \right] \quad (10)$$

In the maximization step (M-step), we maximize the weighted likelihood function with respect to

\mathbf{W} and β . Under the MAP scheme, we assume an isotropic Gaussian prior distribution over \mathbf{W}

$$P(W) = \left(\frac{\alpha}{2\pi} \right)^{\frac{MD}{2}} \exp\left(-\frac{\alpha}{2} \sum_m^M \sum_d^D W_{md}^2\right). \quad (11)$$

Thus, we have two iterative equations for calculating \mathbf{W} and β in the following

$$\sum_n^N \sum_k^K r_{kn}(\Theta^i) \beta_{nd} \varphi_m(\mathbf{x}_k) CTF_{nd} (t_{nd} - CTF_{nd} \sum_m^M \varphi_{m'}(\mathbf{x}_k) W_{m'd}) - \alpha W_{md} = 0 \quad (12)$$

$$\sum_k^K r_{kn}(\Theta^i) \left(\frac{1}{\beta_{nd}} - (t_{nd} - CTF_{nd} \sum_m^M \varphi_m(\mathbf{x}_k) W_{md})^2 \right) = 0 \quad (13)$$

Because of CTF, \mathbf{W} cannot be solved by matrix operations that were previously developed for the GTM framework^{8,9}. We developed a numerical approach to solve a system of linear equations that can be partitioned to many sub-systems of linear equations. In addition, this allows efficient parallelization in a hardware with a broader bandwidth of vectorization. To reduce computational cost, we use a mean β to replace β_{nd}

$$\bar{\beta} = \frac{ND}{\sum_n^N \sum_d^D \beta_{nd}} \quad (14)$$

In the M-step, we have

$$\begin{aligned} \frac{\partial Q(\Theta, \Theta^i)}{\partial W_{md}} &= \sum_n^N \sum_k^K r_{kn}(\Theta^i) (-\beta_{nd}) (t_{nd} - CTF_{nd} \sum_m^M \varphi_{m'}(\mathbf{x}_k) W_{m'd}) (-\varphi_m(\mathbf{x}_k) CTF_{nd}) - \alpha W_{md} \\ &= \sum_n^N \sum_k^K r_{kn}(\Theta^i) \beta_{nd} \varphi_m(\mathbf{x}_k) CTF_{nd} (t_{nd} - CTF_{nd} \sum_m^M \varphi_{m'}(\mathbf{x}_k) W_{m'd}) - \alpha W_{md} = 0 \end{aligned} \quad (15)$$

This is a system of linear equations. Suppose

$$\sum_n^N \sum_k^K r_{kn}(\Theta^i) \beta_{nd} \varphi_m(\mathbf{x}_k) CTF_{nd} t_{nd} = B_{md}$$

In order to see the equations clearly, we suppose $M = 2, D = 3$ for instance. So we have

$$\left(\sum_n^N \sum_k^K r_{kn}(\Theta^i) \beta_{n1} \varphi_1^2(\mathbf{x}_k) CTF_{n1}^2 + \alpha \right) w_{11} + \sum_n^N \sum_k^K r_{kn}(\Theta^i) \beta_{n1} \varphi_1(\mathbf{x}_k) CTF_{n1}^2 \varphi_2(\mathbf{x}_k) w_{21} = B_{11}$$

$$\left(\sum_n^N \sum_k^K r_{kn}(\Theta^i) \beta_{n2} \varphi_1^2(\mathbf{x}_k) CTF_{n2}^2 + \alpha \right) w_{12} + \sum_n^N \sum_k^K r_{kn}(\Theta^i) \beta_{n2} \varphi_1(\mathbf{x}_k) CTF_{n1}^2 \varphi_2(\mathbf{x}_k) w_{22} = B_{12}$$

$$\left(\sum_n^N \sum_k^K r_{kn}(\Theta^i) \beta_{n3} \varphi_1^2(\mathbf{x}_k) CTF_{n2}^2 + \alpha \right) w_{13} + \sum_n^N \sum_k^K r_{kn}(\Theta^i) \beta_{n2} \varphi_1(\mathbf{x}_k) CTF_{n1}^2 \varphi_3(\mathbf{x}_k) w_{23} = B_{13}$$

$$\sum_n^N \sum_k^K r_{kn}(\Theta^i) \beta_{n1} \varphi_2(\mathbf{x}_k) CTF_{n1}^2 \varphi_1(\mathbf{x}_k) w_{11} + \left(\sum_n^N \sum_k^K r_{kn}(\Theta^i) \beta_{n1} \varphi_2^2(\mathbf{x}_k) CTF_{n1}^2 + \alpha \right) w_{21} = B_{21}$$

$$\sum_n^N \sum_k^K r_{kn}(\Theta^i) \beta_{n2} \varphi_2(\mathbf{x}_k) CTF_{n2}^2 \varphi_1(\mathbf{x}_k) w_{12} + \left(\sum_n^N \sum_k^K r_{kn}(\Theta^i) \beta_{n2} \varphi_2^2(\mathbf{x}_k) CTF_{n2}^2 + \alpha \right) w_{22} = B_{22}$$

$$\sum_n^N \sum_k^K r_{kn}(\Theta^i) \beta_{n3} \varphi_2(\mathbf{x}_k) CTF_{n3}^2 \varphi_1(\mathbf{x}_k) w_{13} + \left(\sum_n^N \sum_k^K r_{kn}(\Theta^i) \beta_{n3} \varphi_2^2(\mathbf{x}_k) CTF_{n3}^2 + \alpha \right) w_{23} = B_{23}$$

When we solve w_{11} and w_{21} , we use

$$\left(\sum_n^N \sum_k^K r_{kn}(\Theta^i) \beta_{n1} \varphi_1^2(\mathbf{x}_k) CTF_{n1}^2 + \alpha \right) w_{11} + \sum_n^N \sum_k^K r_{kn}(\Theta^i) \beta_{n1} \varphi_1(\mathbf{x}_k) CTF_{n1}^2 \varphi_2(\mathbf{x}_k) w_{21} = B_{11}$$

$$\sum_n^N \sum_k^K r_{kn}(\Theta^i) \beta_{n1} \varphi_2(\mathbf{x}_k) CTF_{n1}^2 \varphi_1(\mathbf{x}_k) w_{11} + \left(\sum_n^N \sum_k^K r_{kn}(\Theta^i) \beta_{n1} \varphi_2^2(\mathbf{x}_k) CTF_{n1}^2 + \alpha \right) w_{21} = B_{21}$$

If we use

$$\begin{aligned} \vec{w}_1 &= \begin{pmatrix} w_{11} \\ w_{21} \end{pmatrix}, \vec{B}_1 = \begin{pmatrix} B_{11} \\ B_{21} \end{pmatrix} \\ A_1 &= \begin{pmatrix} \sum_n^N \sum_k^K r_{kn}(\Theta^i) \beta_{n1} \varphi_1^2(\mathbf{x}_k) CTF_{n1}^2 + \alpha & \sum_n^N \sum_k^K r_{kn}(\Theta^i) \beta_{n1} \varphi_1(\mathbf{x}_k) CTF_{n1}^2 \varphi_2(\mathbf{x}_k) \\ \sum_n^N \sum_k^K r_{kn}(\Theta^i) \beta_{n1} \varphi_2(\mathbf{x}_k) CTF_{n1}^2 \varphi_1(\mathbf{x}_k) & \sum_n^N \sum_k^K r_{kn}(\Theta^i) \beta_{n1} \varphi_2^2(\mathbf{x}_k) CTF_{n1}^2 + \alpha \end{pmatrix} \end{aligned}$$

For the same situation, we have

$$\begin{aligned} A_2 \vec{w}_2 &= \vec{B}_2 \\ A_3 \vec{w}_3 &= \vec{B}_3 \end{aligned}$$

In a general case, we can numerically solve the D -th system of linear equations $A_d \vec{w}_d = \vec{B}_d$ numerically. Here A_d is $M \times M$ dimensional matrix; \vec{w}_d and \vec{B}_d are M -dimensional vectors.

$$\begin{aligned} A_d \vec{w}_d &= \vec{B}_d \\ \vec{w}_d &= \begin{pmatrix} w_{1d} \\ \vdots \\ w_{Md} \end{pmatrix}, \vec{B}_d = \begin{pmatrix} B_{1d} \\ \vdots \\ B_{Md} \end{pmatrix} \end{aligned} \quad (16)$$

$$A_d = \begin{pmatrix} \sum_n^N \sum_k^K r_{kn}(\Theta^i) \bar{\beta} \varphi_1^2(\mathbf{x}_k) CTF_{nd}^2 + \alpha & \cdots & \sum_n^N \sum_k^K r_{kn}(\Theta^i) \bar{\beta} \varphi_1(\mathbf{x}_k) CTF_{nd}^2 \varphi_m(\mathbf{x}_k) \\ \vdots & \ddots & \vdots \\ \sum_n^N \sum_k^K r_{kn}(\Theta^i) \bar{\beta} \varphi_m(\mathbf{x}_k) CTF_{nd}^2 \varphi_1(\mathbf{x}_k) & \cdots & \sum_n^N \sum_k^K r_{kn}(\Theta^i) \bar{\beta} \varphi_m^2(\mathbf{x}_k) CTF_{nd}^2 + \alpha \end{pmatrix}$$

CTF correction during manifold learning. When the expectation-maximization algorithm is converged, one can obtain the probability that the n -th data point was generated by k -th latent variable. A rigorous equation for calculating 2D class average was derived from the above-described mathematical framework as

$$A_{kd} = \frac{\sum_{n=1}^N r_{kn}(\Theta) \beta_{nd} CTF_{nd} t_{nd}}{\sum_{n=1}^N r_{kn}(\Theta) \beta_{nd} CTF_{nd} t_{nd}^2 + \alpha}. \quad (17)$$

The expression resembles the Wiener-type filter and gives rise to CTF-corrected, probability-weighted class averages.

Implementation of the SML algorithm. We implemented the following algorithm in ROME.

Set the number of latent conformation points $\{x_k\}$, $k = 1, 2, 3 \dots K$

Set the value of basis function centers $\{\mu_m\}$, $m = 1, 2, 3 \dots M$

Select the value of basis function width σ

Calculate the basis function φ from equation (4)

Initialize weighted matrix \mathbf{W} from Gaussian circle and the standard deviation of noise β

Repeat

E-step:

Compute the δ_{nd} distance between latent space and data space

$$\delta_{nd} = (t_{nd} - CTF_{nd} \sum_{m=1}^M \varphi_m(x_k) W_{md})^2, \text{ from equation (2)}$$

Compute probability matrix P from equation (6) using φ , δ_{nd} and \mathbf{W}

Compute responsibility matrix R from equation (9) using P , δ_{nd} and \mathbf{W}

M-step:

Using equation (16) and R to update \mathbf{W}

Use R and δ_{nd} to update β_{nd} from equation (13)

Until convergence

Calculate class averages from equation (17).

Protocols in deep classification. Two strategies of deep classification have been designed. First, all particles are aligned based on the translations and rotations determined by MAP. Then GTM is applied to partition these shifted and rotated particles into different subsets. CTF is corrected during class averaging similar to the Wiener filter. This first strategy is used for obtaining deep classification quickly in several hours. However, some class might be mixed with un-identical conformational states. Thus, in the second strategy, the dataset is initially classified into tens to

hundreds of classes and some classes are further classified into tens to hundreds of reference-free sub-classes per class, depending on the particle population of each class. Aligned particles of each subset are processed by GTM classifier alone. CTF is corrected during class averaging. These two strategies can be used in different cases. If plenty of classes are needed to assess sample heterogeneity, the first strategy can be used to obtain relative more unsupervised classes without any human intervention. However, if more sub-classes are needed for some subsets, the second one can provide more details of specific subsets to examine structural heterogeneity.

Experimental data used in the test. Three experimental cryo-EM data were collected from an FEI Tecnai Arctica microscope, operated under an acceleration voltage of 200 kV and equipped with Gatan K2 Summit direct electron detector. Inflammasome and 26S proteasome were imaged at a nominal magnification of 21,000 times, while 19S RP were imaged at a nominal magnification of 54,000 times. Cryo-EM data were collected semi-automatically by the Legion. Movies of 36 frames per exposure were collected for inflammasome (an accumulated dose of 47.6 electrons/Å²) and free 19S RP (an accumulated dose of 50 electrons/Å²). For 26S proteasome, movies of 30 frames per exposure and an accumulated dose of 30 electrons/Å² were obtained. The physical pixel size and the super-resolution pixel size of inflammasome and 26S proteasome datasets are 1.72 Å and 0.86 Å, respectively. The calibrated physical pixel size of 19S RP is 0.98 Å. The defocus in data collection were all set in the range of from -1.0 to -3.0 μm.

Comparison with other approaches. 281 particles in one side-view class of 11-fold complexes (green box in Fig. 2c) were selected to test the performance of unsupervised classification in

ROME, compared with reference-free MAP classification in RELION and K-means clustering in SPIDER. 50 classes were generated on these three software. First, all images divided into 50 classes using ROME. Some classes indicate mis-classification of the side views of 10-fold complex in this group as dictated from the length difference (red box in Supplementary Fig. 3a). Some classes might also exhibit an incomplete inflammasome complex (green box in Supplementary Fig. 3a). Second, 2D classification for 50 classes was executed using RELION. Unfortunately, only one major class is returned to represent the side view of 11-fold complex and no side views of 10-fold complex are found (Supplementary Fig. 3b). We also did unsupervised 2D classification into 50 classes by K-means clustering in SPIDER. All particles were firstly corrected with CTF function. Then the low-pass filtered particles were aligned in a reference-free manner in SPIDER. Next, all images were partitioned by unsupervised K-means clustering algorithm. Finally, class averages were obtained by averaging particles in each class, respectively. The projection structures in some class averages were shorter than others, indicating that 10-fold complex particles are hidden within this data group (red box in Supplementary Fig. 3c). However, many class average indicates mis-classification or mis-alignment of the images (green box in Supplementary Fig. 3c).

Implementation and code optimization on Intel® Xeon® processors and Intel® Xeon Phi™ coprocessors. Both MAP and SML/GTM implementations are optimized in ROME. Similar to MAP in RELION, algorithm-level optimizations such as adaptive expectation-maximization have been adopted in ROME. In additional optimizations, the particle image stack is divided based on the unit of individual images across the computer nodes in the parallelization of data flow in the MAP module. However, the image stack is divided based on the unit of individual

image pixels in SML/GTM module. This allowed the problem to be distributed between multiple cluster nodes and attached coprocessors, while minimizing data transfer and memory requirements. Second, by simplifying the calculation of \mathbf{W} and using a mean β in place β_{nd} (equations 11-14), the memory and compute requirements of the algorithm were considerably reduced (although still very high). Next, complex data structures were converted from arrays of structures into structures of arrays to make it easier to implement the inner loops of compute-intensive kernels with processor instructions that can execute on multiple data elements in parallel (vectorization). Loops were also restructured so that independent threads of execution worked on data elements that were near each other in memory. This “cache blocking” attempts to lower the pressure the algorithms put on the memory subsystem as the number of threads climb, and tries to make the most effective use of the processor memory caches. To further improve the use of memory and decrease serializing overhead, memory allocation and deallocation were moved from the middle of the algorithm to an initialization phases. Finally, we used single-precision data types instead of double-precision for storing image data in parts of the algorithm where the extra accuracy was not necessary. This treatment has the potential to double performance.

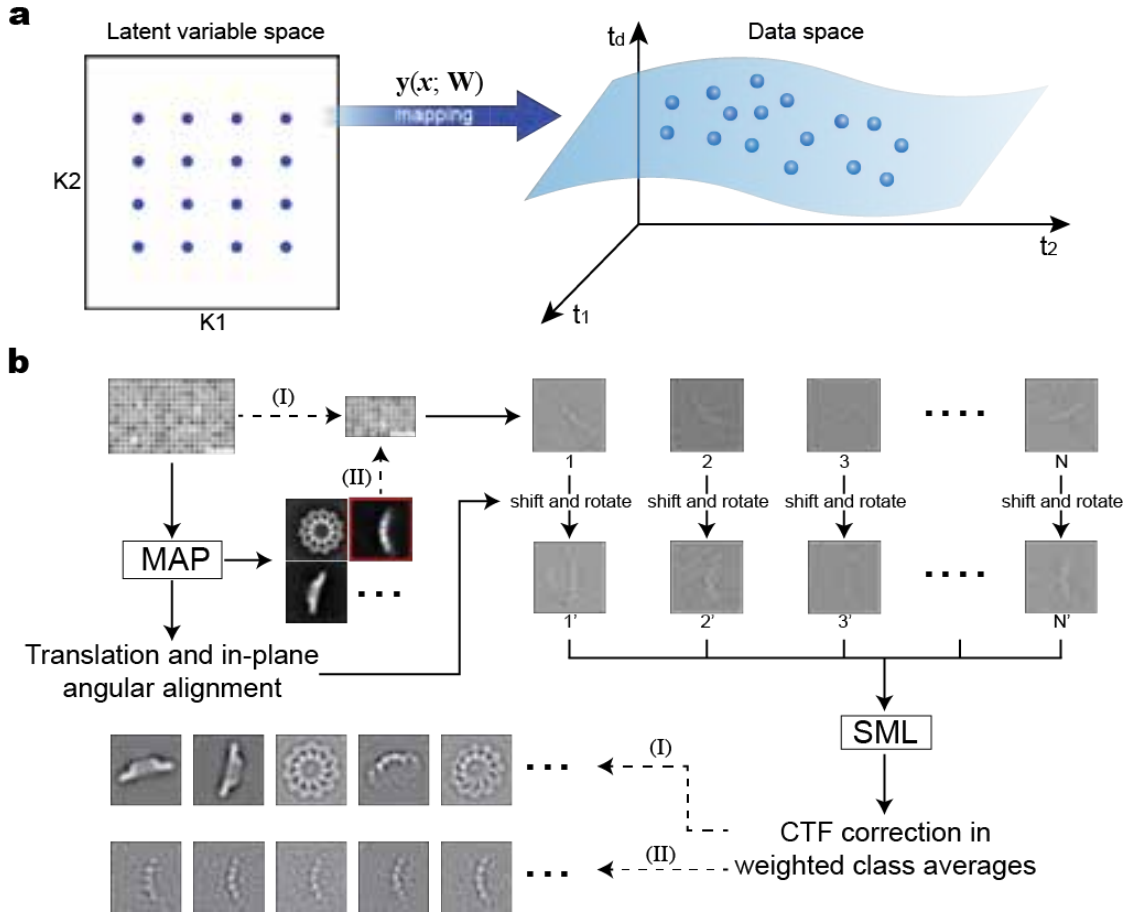


Figure 1. Strategy of unsupervised deep classification by statistical manifold learning. a,

The fundamental principle of SML is to establish the numerical relationship between variables in latent space and a non-Euclidean manifold composed of the Fourier transformed image data in D -dimensional data space. The manifold embedding can be determined by a set of nonlinear basis functions and a weighted parametric matrix. The likelihood function for the nonlinear mapping is solved by expectation-maximization method. **b,** The work flow of two deep

classification strategies in ROME. (I) All images were aligned through MAP in a reference-free manner and then classified into a large number of groups by unsupervised SML. (II)

Unsupervised classes were further classified into many sub-classes by unsupervised SML. Initial supervised classification can be done by either MAP or SML.

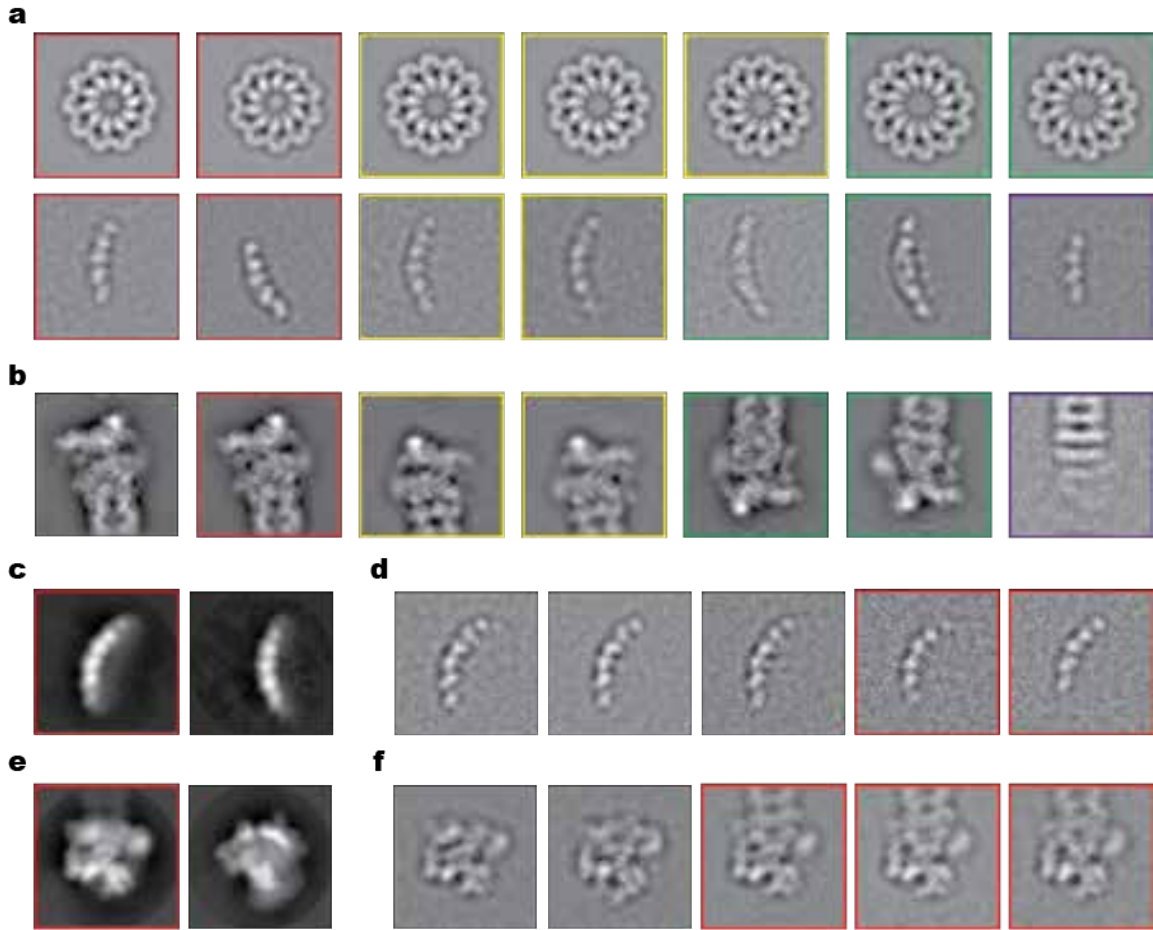


Figure 2. Unsupervised classification by SML. a, A 17,103-particle dataset of inflammasome was classified with unsupervised SML in ROME. After alignment by MAP, three hundred classes were generated. Only top fourteen most particles class averages were shown. CTF-corrected class averaging exhibit different views of inflammasome complex. In the first row, red, yellow and green boxes indicate the top views (the first row) and the side views (the second row) of 10-fold, 11-fold, and 12-fold inflammasome complex, respectively. The side views of the complex structure differ by length. The purple box exhibits a class average of an incomplete inflammasome complex. **b,** A 96,488-particle dataset of RP-CP sub-complex was classified with unsupervised SML in ROME. Only top seven classes with the most particles among three

hundred classes were shown. The red box or yellow box label a pair of class averages showing difference in local feature corresponding to the local movement of Rpn5 subunit of RP-CP subcomplex. The green box labels a pair of class averages showing the movement of Rpn1 subunit of RP-CP subcomplex. The purple box exhibits a class average of an incomplete RP-CP subcomplex. **c**, A 16,306-particle dataset of inflammasome were initially classified with MAP classifier in a reference-free manner. Two classes among 50 classes visually looked like 11-fold inflammasome complex particles. **d**, 843 particles of one class, whose average is highlighted by red box in panel **c** were further classified by SML. The red box indicates the 10-fold inflammasome particles that are mis-classified by MAP into the same class as the rest 11-fold structures. **e**, A 57,001-particle dataset of free RP were initially classified with MAP classifier in a reference-free manner. Most free RP complex and RP-CP subcomplex particles can be distinguished by 2D class averaging. Some mixed classes (red box) also exist. **f**, 3,961 particles in one class in RP dataset (marked by red box in panel **e**) were further classified by SML in ROME. 448 RP-CP subcomplex particles were found to be misclassified into this free RP class.

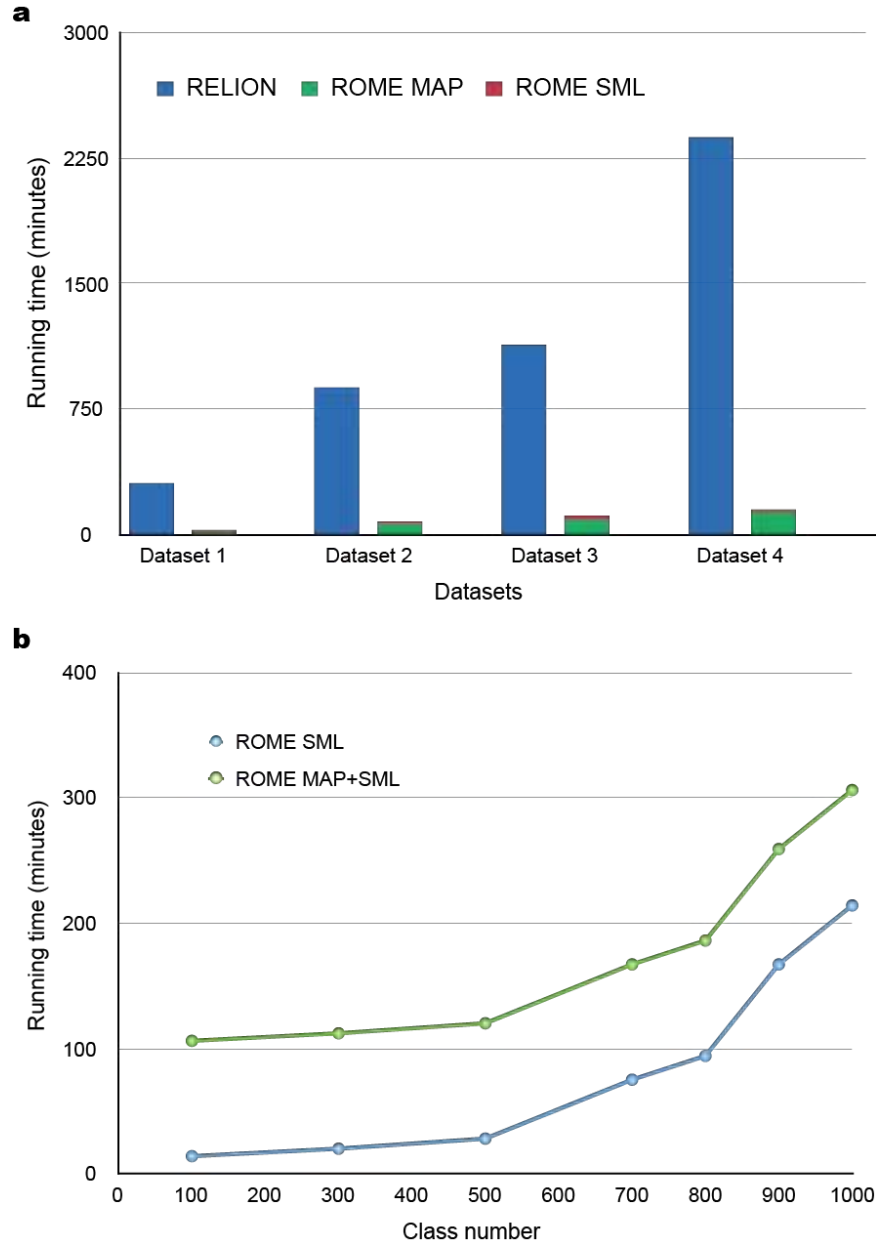


Figure 3. Performance evaluation of unsupervised deep classification with ROME. a, Performance of unsupervised classification in ROME versus RELION through different data. Unsupervised 2D classification into 300 classes based on RELION were performed on 4 experimental data, while MAP alignment in ROME and SML classification for 300 classes were also performed. The blue histogram represents the running time of RELION (Fig. 3b). The green

histogram represents the running time of MAP in ROME, and the red histogram represents the time of SML. **b**, A 96,488-particle dataset of RP-CP subcomplex particles boxed by 180x180 were used to test the performance of SML in ROME (blue dots). Together with 92-minute alignment by MAP in ROME, the green dots represent the total running time including both alignment and classification in ROME. The running time is polynomial related to class number.

References

1. Nogales, E. The development of cryo-EM into a mainstream structural biology technique. *Nat Methods* **13**, 24-27 (2016).
2. Frank, J. Three-dimensional electron microscopy of macromolecular assemblies : visualization of biological molecules in their native state, Edn. 2nd. (Oxford University Press, Oxford ; New York; 2006).
3. Scheres, S.H. et al. Disentangling conformational states of macromolecules in 3D-EM through likelihood optimization. *Nat Methods* **4**, 27-29 (2007).
4. Zhang, L. et al. Cryo-EM structure of the activated NAIP2-NLRC4 inflammasome reveals nucleated polymerization. *Science* **350**, 404-409 (2015).
5. Sigworth, F.J. A maximum-likelihood approach to single-particle image refinement. *J Struct Biol* **122**, 328-339 (1998).
6. Scheres, S.H. et al. Maximum-likelihood multi-reference refinement for electron microscopy images. *J Mol Biol* **348**, 139-149 (2005).
7. Scheres, S.H. A Bayesian view on cryo-EM structure determination. *J Mol Biol* **415**, 406-418 (2012).
8. Bishop, C.M., Svensen, M. & Williams, C.K.I. GTM: the generative topographic mapping. *Neural Computation* **10**, 215-234 (1998).
9. Bishop, C.M., Svensen, M. & Williams, C.K.I. Developments of the generative topographic mapping. *Neurocomputing* **21**, 203-224 (1998).
10. Gorban, A.N. Principal manifolds for data visualization and dimension reduction. (Springer, Berlin; 2008).
11. Jeffers, J. & Reinders, J. Intel Xeon Phi coprocessor high-performance programming. (Elsevier ; Morgan Kaufmann, Amsterdam ; Boston; 2013).
12. Allinson, N. Advances in self-organising maps. (Springer, London ; New York; 2001).
13. Tagare, H.D., Barthel, A. & Sigworth, F.J. An adaptive Expectation-Maximization algorithm with GPU implementation for electron cryomicroscopy. *J Struct Biol* **171**, 256-265 (2010).
14. Scheres, S.H. RELION: implementation of a Bayesian approach to cryo-EM structure determination. *J Struct Biol* **180**, 519-530 (2012).
15. Shaikh, T.R. et al. SPIDER image processing for single-particle reconstruction of biological macromolecules from electron micrographs. *Nat Protoc* **3**, 1941-1974 (2008).